Received: 28 November 2017 | Revised: 13 January 2018 | Accepted: 29 January 2018

DOI: 10.1002/er.4032

RESEARCH ARTICLE

WILEY INTERNATIONAL JOURNAL OF ENERGY RESEARCH

Novel radioluminescent nuclear battery: Spectral regulation of perovskite quantum dots

Wang Chen[1] | Xiaobin Tang[1,2] | Yunpeng Liu[1,2] | Zhiheng Xu[1] | Zhenyang Han[1] | Zhengrong Zhang[1] | Hongyu Wang[1] | Cong Peng[1]

[1] Department of Nuclear Science and Engineering, Nanjing University of Aeronautics and Astronautics, Nanjing 211106, China

[2] Jiangsu Key Laboratory of Material and Technology for Energy Conversion, Nanjing 211106, China

Correspondence
Tang Xiaobin, Department of Nuclear Science and Engineering, Nanjing University of Aeronautics and Astronautics, Nanjing 211106, China.
Email: tangxiaobin@nuaa.edu.cn

Funding information
National Natural Science Foundation of China, Grant/Award Number: 11505096 and 11675076; Natural Science Foundation of Jiangsu Province, Grant/Award Number: BK20150735; Shanghai Aerospace Science and Technology Innovation Project, Grant/Award Number: SAST2016112; Foundation of Graduate Innovation Center in NUAA, Grant/Award Number: kfjj20170611; Priority Academic Programme Development of Jiangsu Higher Education Institutions

Summary

$CsPbBr_3$ and $CsPbBr_{1.5}I_{1.5}$ perovskite quantum dots (QDs) are synthesized by hot-injection with PPO (2,5-diphenyloxazole) as a fluorescent material for radioluminescent nuclear battery. The results reveal that the fluorescence of the QD/PPO system consists of radioluminescence (4.79%-5.35%) and photoluminescence (nearly 95%). The addition of QDs leads to more excellent optical and electrical properties of radioluminescent nuclear battery. The peak position of the radioluminescence spectra of QD/PPO can be regulated by controlling the components of QDs. This strategy is suitable for obtaining a satisfactory spectral matching factor for different photovoltaic devices to obtain outstanding output performance. Moreover, good selection of QD/PPO as a fluorescent material can significantly improve the overall output performance of the radioluminescent nuclear battery. The linear relationship between optical and electrical properties was presented. Perovskite QDs exhibit excellent application prospects for the (α, β, γ, and X-ray sources) radioluminescent nuclear battery and X-ray imaging technology.

KEYWORDS

nuclear battery, perovskite quantum dots, radioluminescence, spectral regulation

1 | INTRODUCTION

Microelectromechanical systems (MEMS) have developed rapidly in recent decades. Microelectromechanical systems devices pursue smaller size and higher power. Due to bulky, short-life, poor adaptability to the environment, traditional fuel cells and solar cells are unable to satisfy the power requirements of MEMS devices.[1-3]

Nuclear batteries, which convert the decay energy of radioisotopes into electrical energy, are a potential candidate for MEMS energy supplies. Increasing the activity and choosing a radioactive source of high-energy are the most direct ways to improve the output performance of nuclear cells to meet the power requirements of MEMS. Previous studies have shown that the particles (α, β, γ, and X-ray) decayed from the radioactive source can easily make radiation damage on the semiconductor for the radiovoltaic nuclear battery with direct energy conversion.[4,5]

As an indirect energy conversion, a radioluminescent nuclear battery consists of a radioactive source, a fluorescent material, and a photovoltaic (PV). Since the radiation damage of semiconductors in direct energy conversion, radioluminescent nuclear battery is expected to be used in radioactive sources of high activity and energy, which has been widely studied.[6-10] However, the existing radioluminescent nuclear battery exhibits low output power and energy conversion efficiency because of the unsatisfactory matching between the fluorescent material and the PV

cells. Therefore, a new fluorescent material is sought to regulate the emission spectrum to match the peak of the external quantum efficiency curve of the different PV, to obtain a more excellent battery output performance.

Perovskite quantum dots (QDs) and traditional QDs in the light-emitting diode, solar cells, sensors, and other fields have made rapid development.[11,12] Kovalenko et al[13] reported that $CsPbX_3$ (X = Cl, Br, and I) QDs exhibit high photoluminescence (PL) efficiency (~90%) and narrow full width at half maximum (FWHM), which is superior to that of most traditional QDs. Valais et al[14] demonstrated that the CdSe/ZnS QDs exhibit great potential for X-ray detection. In 2017, Chen et al[15] studied the radioluminescence (RL) of $CsPbBr_3$ perovskite QDs under X-ray. The results show that the $CsPbBr_3$ perovskite QDs are liable to be regulated emission spectra and demonstrate a potential application on scintillator detectors and radioluminescent nuclear battery. Manna et al[16] reported in 2016 that X-ray irradiation could improve the stability of perovskite QDs. Related research studies on X-ray source nuclear battery are also being more and more widespread.[17-20]

In this paper, the combination of QDs and 2,5-diphenyloxazole (PPO) was predicted to enhance the emission intensity as well as regulate the emission spectrum. The overall output performances of the battery before and after the spectral regulation were studied. The results show that using perovskite QDs for spectral regulation can greatly improve the overall output performance of the radioluminescent battery. The feasibility of using perovskite QDs in radioluminescent nuclear battery was also verified. There is also a great potential for (a, β, γ, and X-ray) radioluminescent nuclear battery and X-ray imaging technology.

2 | MATERIALS AND METHODS

2.1 | Synthesis of $CsPbX_3$ QDs and $CsPbX_3$ QD/PPO

$CsPbBr_3$ and $CsPbBr_{1.5}I_{1.5}$ QDs were synthesized by hot-injection with oleylamine and oleic acid as surfactants.[13] Surface alkyl promoted the dispersion of $CsPbX_3$ QDs in an organic solvent and disperses $CsPbX_3$ QDs in toluene.[15]

2,5-Diphenyloxazole was dissolved in toluene solvent to obtain different solution concentrations (1-6 mg/mL) for measurement of RL intensity under a fixed tube voltage of 60 kV and tube current of 800 μA. The optimal concentration of the PPO solution was determined as 2 mg/mL (Figure S1). $CsPbX_3$ QD/PPO solution was obtained by adding 20 mg PPO powders into 10 mL QD solution, and then was operated magnetic stirring until fully dissolved. The mass concentrations of QD/PPO and QD solutions configured in this paper are both 10 mg/mL (synthesis details were represented in the Supporting Information).

2.2 | Experimental methods

2.2.1 | X-ray tube energy spectra measurement

The X-ray spectrum of the X-ray tube (Shanghai KeyWay Electron Company Ltd. KYW900A, China) at different tube power levels (10-60 kV) were measured by using a hemispherical CZT radiation probe (Shanxi Imdetek Company Ltd DT-01C1, China) and ORTEC digital multichannel (ORTEC 572A/672, USA). The CZT radiation probe and the X-ray beam were collimated by lead (Pb). X-rays are hardened by 2 mm aluminum plates. The specific parameters of the X-ray tube are shown in Table 1. The obtained X-ray spectra information and the test system are shown in Figure 2.

2.2.2 | PL and absorption spectra measurement

Ultraviolet (UV)/Vis absorption spectra were recorded by using a UV/Vis spectrophotometer (Varian Cary 100, USA), and the PL spectra of the QDs were obtained by using a fluorescence spectrometer (Cary Eclipse Spectrometer, Agilent Technologies Inc., Malaysia).

2.2.3 | RL spectrum measurement

The RL emission spectra of the $CsPbX_3$ QD solutions were measured and characterized to determine the characteristic emission peaks of the solvent and solute. The X-ray source was an X-ray tube with Mo target and operated at10 to 60 kV and 100 to 1000 μA. Emission spectrum was recorded at 200 to 1000 nm by using a fluorescence spectrophotometer (Cary Eclipse Spectrometer, Agilent

TABLE 1 Specific parameters of the X-ray tube

Anode Voltage	Anode Current	Maximum Power	Filament Voltage	Filament Characteristic
60 kV	0-1 mA	65 W	2.0 V	$I_f \approx 1.7$ A
Thickness of beryllium window	Target angle	Focus spot size	Grounded mode	Target
200 μm	10°	0.1 mm × 0.1 mm	Grounded cathode	Molybdenum

Technologies Inc., Malaysia). The slit width of the emission monochromator was set to 20 nm, and the tube voltage of photomultiplier was set to 800 V.

2.2.4 | High-resolution transmission electron microscopy

One drop of $CsPbX_3$ QD solution was dispersed onto a Cu grid. High-resolution transmission electron microscopy (HRTEM) images were obtained on a Tecnai G2 F30 S-TWIN instrument.

2.2.5 | Measurement of the optical property of radioluminescent nuclear battery

Radioluminescence was imaged by using an electron-multiplying charge-coupled device (EMCCD) camera (Andor iXon Ultra 888#BV, USA) equipped with a Canon EF 24 to 70 mm f/2.8 L II USM zoom lenses. The integration time for all images was set to 1 second. The image resolution was 1024 × 1024 active pixels. Raw images were processed by subtracting a background image that was obtained under the same lighting conditions but turned off X-ray tube. All instruments were in the Faraday dark box during the experiments. Reproducibility was tested by recording 3 consecutive images for each measurement and then the standard deviation of each test result were calculated (Tables S1–S3). The camera and some test samples are shown in Figure 1B).

2.2.6 | Measurement of electrical property of radioluminescent nuclear battery

Current-voltage curve was measured by a dual-channel system source-meter instrument (Keithley 2636A, USA). The instrument and some test samples are shown in Figure 1C.

The physical diagrams of the optical and electrical measurement systems are shown in Figure 1.

3 | RESULTS AND DISCUSSION

3.1 | X-ray tube energy spectra measurement

The X-ray spectra of the X-ray tube at different tube power (10-60 kV) were recorded by using a CZT radiation probe and ORTEC digital multichannel (Figure 2).

An X-ray tube uses high-speed electron impact on the metal target bremsstrahlung to produce X-ray. The tube

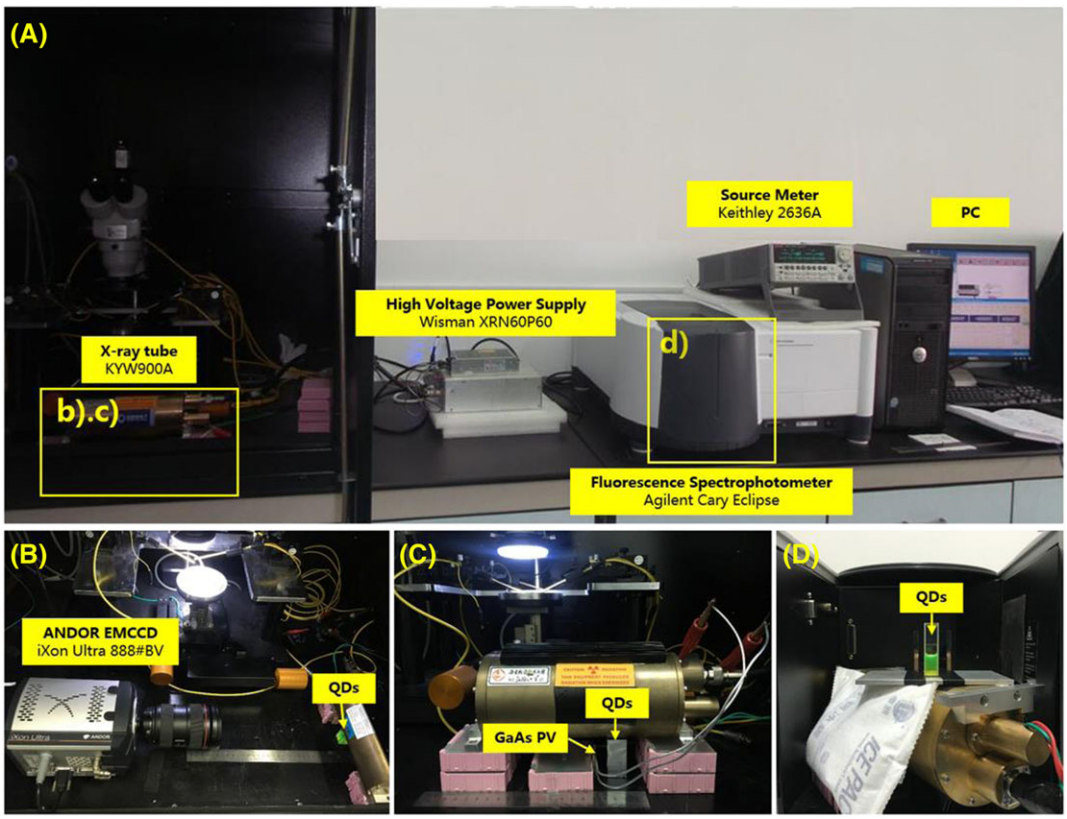

FIGURE 1 A, Physical diagram of the measurement system; B, radioluminescence image test system (electron-multiplying charge-coupled device); C, Electrical property test system (2636A); and D, radioluminescence spectrum test system [Colour figure can be viewed at wileyonlinelibrary.com]

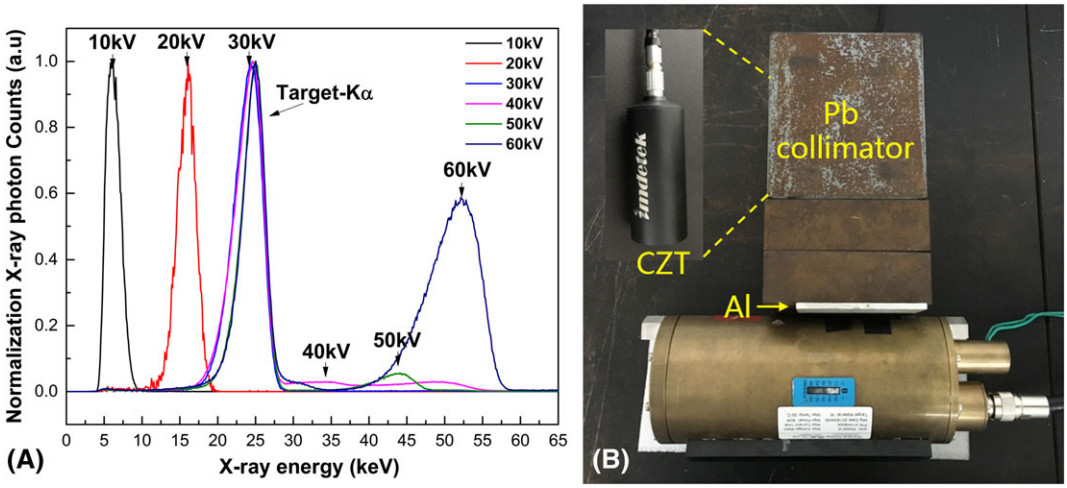

FIGURE 2 A, X-ray tube energy spectra with CZT detector. B, Physical diagram of X-ray tube energy spectrum test system [Colour figure can be viewed at wileyonlinelibrary.com]

voltage can be adjusted so that the accelerated electrons can obtain different average energy levels and energy X-ray. The X-ray spectra show that adjusting the X-ray tube voltage can regulate the emitted X-ray energy and can be used for equivalent different low-energy X-ray sources.

3.2 | Characterization of $CsPbX_3$ QDs

3.2.1 | Optical property of colloidal $CsPbX_3$ QDs

The PL spectra and the typical optical absorption of $CsPbBr_3$ QDs and $CsPbBr_{1.5}I_{1.5}$ QD solutions with identical concentrations (10 mg/mL) are presented in Figure 3.

The peak position and the FHWM of the PL spectra of $CsPbBr_3$ QDs and $CsPbBr_{1.5}I_{1.5}$ QDs are 515.9, 619.8, 10.2, and 16.1 nm (Table 2). In contrast to those of traditional fluorescent materials, the peak position and FWHM of the perovskite QD emission spectrum can be easily regulated by changing the QD composition. Perovskite QDs can achieve full spectrum control in the visible range.

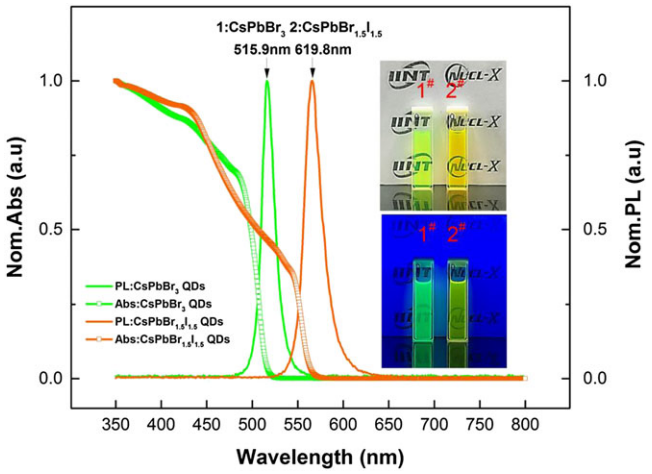

FIGURE 3 Photoluminescence (PL) spectra (λ_{exc} = 350 nm for all samples) and typical optical absorption of perovskite $CsPbBr_3$ quantum dots (QDs) and $CsPbBr_{1.5}I_{1.5}$ QDs in toluene; illustration for the samples under ultraviolet lamp (λ = 365 nm) and visible light [Colour figure can be viewed at wileyonlinelibrary.com]

3.2.2 | HRTEM of colloidal $CsPbX_3$ QDs

The HRTEM images and the results of the particle size analysis of $CsPbBr_3$ QDs and $CsPbBr_{1.5}I_{1.5}$ QDs are presented in Figure 4.

The HRTEM images show the distinct particle sizes of the 2 synthesized QDs. The difference in the reaction conditions during synthesis primarily results from the difference in the emission peak positions of the PL and RL spectra of the 2 different QDs (Figures 3 and 12). The HRTEM images show that the resulting particle sizes are 7.08 nm for $CsPbBr_3$ QD and 8.33 nm for $CsPbBr_{1.5}I_{1.5}$ QDs, respectively.

3.3 | Optical property of radioluminescent nuclear batteries

The RL images of different types of fluorescent materials ($CsPbBr_3$ QDs, $CsPbBr_{1.5}I_{1.5}$ QDs, PPO, $CsPbBr_3$ QD/PPO, and $CsPbBr_{1.5}I_{1.5}$ QD/PPO each 5 mL) were obtained by using an EMCCD camera under different X-ray irradiation conditions, as shown in Figure 5.

The image resolution was set to 1024 × 1024 active pixels. Raw images were processed by subtracting a background image that was obtained under the same lighting conditions with turned off X-ray tube. Reproducibility was tested by recording 3 consecutive images for each measurement, and the standard deviations of each test result were then calculated (Tables S1–S3). The QD/PPO

TABLE 2 The QD/PPO and PPO SMF of EMCCD and GaAs PV

	EMCCD, %	GaAs, %	PEAK, nm	FHWM, nm
PPO	42.48	36.76	371.5	54.2
$CsPbBr_3$ QD/PPO	91.74	88.34	515.9	10.2
$CsPbBr_{1.5}I_{1.5}$ QD/PPO	95.44	92.38	619.8	16.1

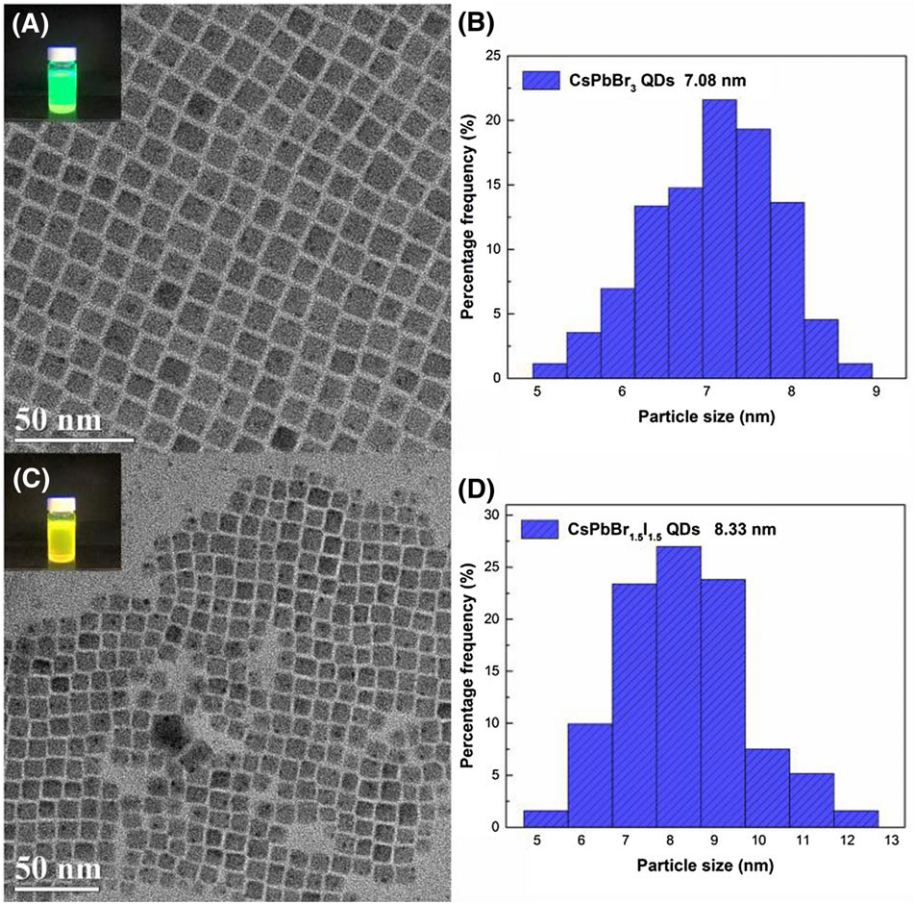

FIGURE 4 High-resolution transmission electron microscopy images and particle size distribution of (A and B) $CsPbBr_3$ quantum dot (QD) and (C and D) $CsPbBr_{1.5}I_{1.5}$ QDs, illustration for the samples under ultraviolet lamp ($\lambda = 365$ nm) [Colour figure can be viewed at wileyonlinelibrary.com]

system captured by EMCCD produced significantly more count information than the PPO system. Figure 6 shows the count statistics of different solution RL images under different radiation conditions.

Based on the results of the statistical counting, the PL and RL of the QDs relative to the total fluorescence of the QD/PPO system can be calculated according to Equations 1, 2, and 3.

$$K_1 = \frac{\mathrm{ROI(QDs/PPO)}}{\mathrm{ROI(PPO)}}, \tag{1}$$

$$\mathrm{RL_{ratio}} = K_2 = \frac{\mathrm{ROI(QDs)}}{\mathrm{ROI(QDs/PPO)}}, \tag{2}$$

$$\mathrm{PL_{ratio}} = 1 - K_2, \tag{3}$$

where K_1 is equal to the counts of QD/PPO [ROI(QD/PPO)] divided by the counts of PPO and reflects the multiples of QDs/POO counts relative to PPO counts [ROI(PPO)] with and without additional QDs. K_2 is equal to the counts of QDs [ROI(QDs)] divided by the counts of QD/PPO and reflects the share of QDs RL to the total fluorescence in the QD/PPO system. The terms of K_1 and K_2 under different X-ray irradiation environments have been represented in Figure 7.

The fluorescence counts of QD/PPO system are larger than QD system or PPO system. The fluorescence counts

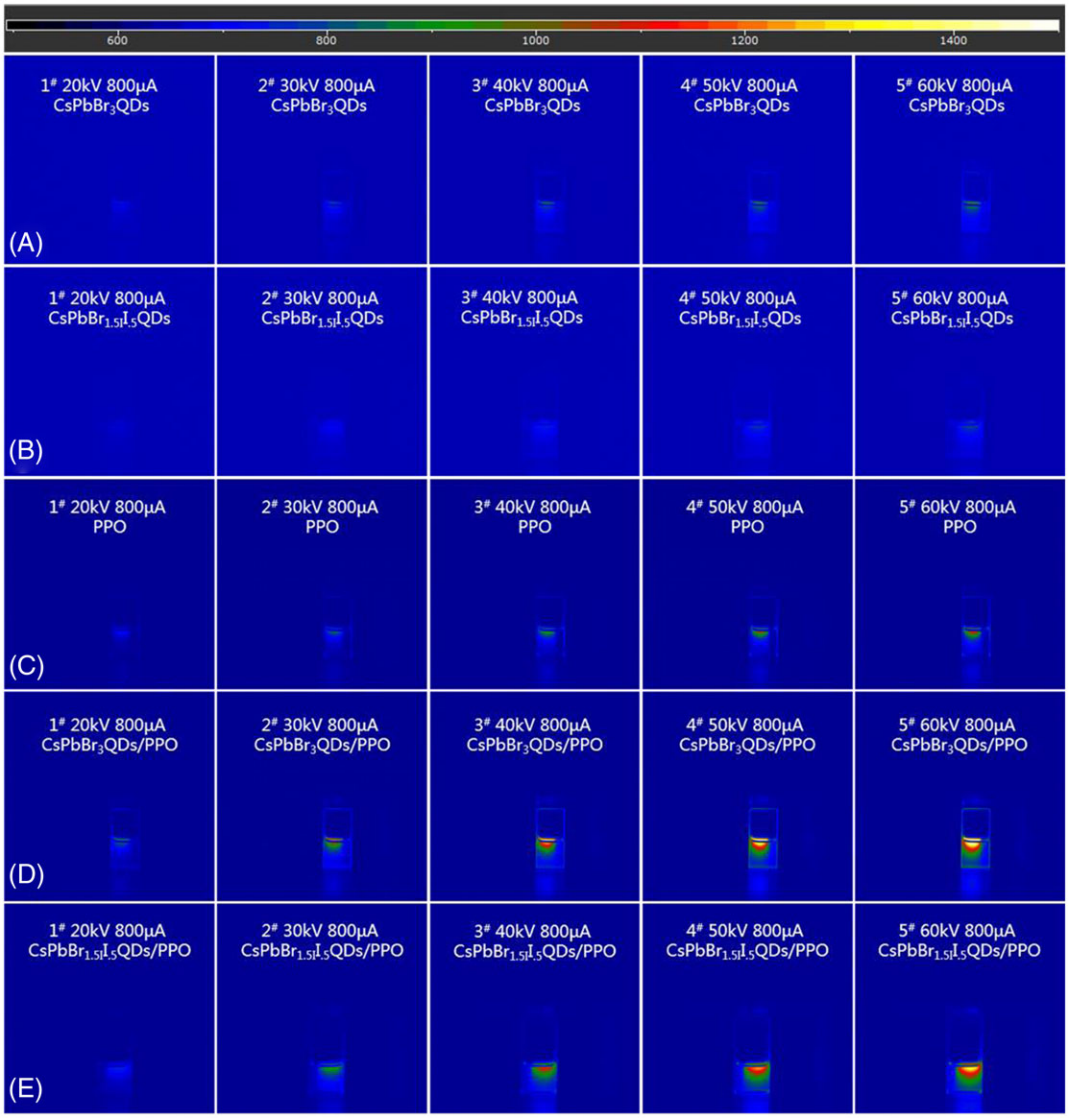

FIGURE 5 Image taken by the electron-multiplying charge-coupled device A, $CsPbBr_3$ quantum dots (QDs), B, $CsPbBr_{1.5}I_{1.5}$ QDs, C, PPO, D, $CsPbBr_3$ QD/PPO, and E, $CsPbBr_{1.5}I_{1.5}$ QD/PPO under different X-ray irradiation conditions (tube voltage 60 kV and tube current of 800 μA) [Colour figure can be viewed at wileyonlinelibrary.com]

of the QD/PPO system are approximately 2.36 to 2.83 times higher than that of PPO system. According to EMCCD statistical countings, it can be seen that the QD/PPO systems produce 4.79% to 5.35% of RL and nearly 95% of PL. The fluorescence counts of the $CsPbBr_3$ QD/PPO system are slightly higher than that of the $CsPbBr_{1.5}I_{1.5}$ QD/PPO system because of its higher fluorescence quantum efficiency.

3.4 | Electrical property of radioluminescent nuclear batteries

GaAs single-junction PV devices were used as energy conversion units to absorb the RL and produce an electrical output. The detailed structure of GaAs PV is shown in Figure 8B. Radioluminescent nuclear batteries are typically characterized through their electronic performance parameters such as short-circuit current (I_{sc}), open-circuit voltage (V_{oc}), maximum output power (P_{max}), and fill factor (FF). The physical and *I-V* curves showed in Figures 8 and 9. The voltage and current at the maximum power point were denoted as I_{mp} and V_{mp}, respectively. P_{max} was calculated as follows:

$$P_{max} = V_{mp} I_{mp} \tag{4}$$

$$FF = \frac{P_{max}}{V_{oc} I_{sc}} \tag{5}$$

At the I_{sc} and V_{oc} points, the power is 0 and the P_{max} occurs between the 2 terms. FF is the ratio of the P_{max} to the product of the I_{sc} and fs_{oc}.

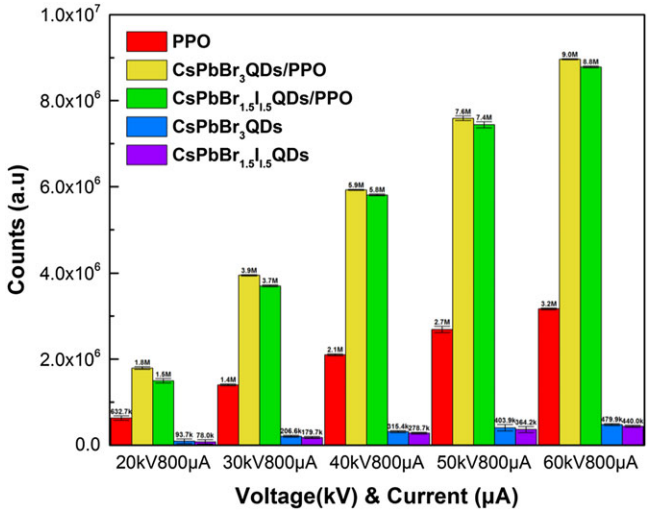

FIGURE 6 Counting statistics of radioluminescence images of different solutions taken by electron-multiplying charge-coupled device under different radiation conditions [Colour figure can be viewed at wileyonlinelibrary.com]

The *I-V* and *P-V* curves of the radioluminescent nuclear battery with different fluorescent materials (including $CsPbBr_3$ QD/PPO, $CsPbBr_{1.5}I_{1.5}$QD/PPO, and PPO) were measured by the above experimental method (Figures 9 and 10). The differences in the electrical properties of the entire nuclear battery before and after the addition of QDs were compared.

The electrical properties of the QD/PPO system obtained from the *I-V* and *P-V* curves are significantly better than those of the PPO system under different X-ray irradiation conditions. The electrical properties of $CsPbBr_3$ QD/PPO system are superior to those of the $CsPbBr_{1.5}I_{1.5}$ QD/PPO system, consistent with the characterization of previous optical properties. The values of I_{sc}, V_{oc}, P_{max}, and FF of the QD/PPO and PPO radioluminescent nuclear batteries were calculated from the data in the *I-V* curves and the *P-V* curves by using the Equations 4 and 5 (Figure 10).

The V_{oc}, I_{sc}, P_{max}, and FF of PPO radioluminescent nuclear battery were all set at 1 for a reference. Figure 11 shows the corresponding coefficients of the electrical parameters of the QD/PPO nuclear radioluminescent batteries with respect to the PPO nuclear radioluminescent batteries one.

Compared with the electrical properties of the PPO radioluminescent nuclear battery, those of the QD/PPO radioluminescent nuclear battery have been significantly improved. The most concerned of P_{max} increased to 3.97 to 2.51 times. Optical properties of the QD/PPO system are nearly 2.36–2.83 times larger than that of PPO system. For the radioluminescent nuclear battery, the addition of QDs makes the radioluminescent nuclear battery obtain more excellent optical and electrical properties.

3.5 | Spectral matching factor of QD/PPO and PPO with EMCCD and GaAs

The normalized RL spectra of QD/PPO system and PPO system were measured under different X-ray irradiation conditions, as showed in Figure 12. The spectral compatibility of the QD/PPO and PPO RL with the spectral sensitivity of various optical photon detectors (including EMCCD and GaAs PV), which can be estimated by the spectral matching factor (SMF)[20]:

$$\mathrm{SMF} = \frac{\int S_p(\lambda) S_D(\lambda) d\lambda}{\int S_p(\lambda) d\lambda} \tag{6}$$

where S_P is the RL spectra of the QD/PPO and PPO, S_D is the spectral sensitivity of the EMCCD, GaAs PV, and λ denotes the wavelength of the light. The above

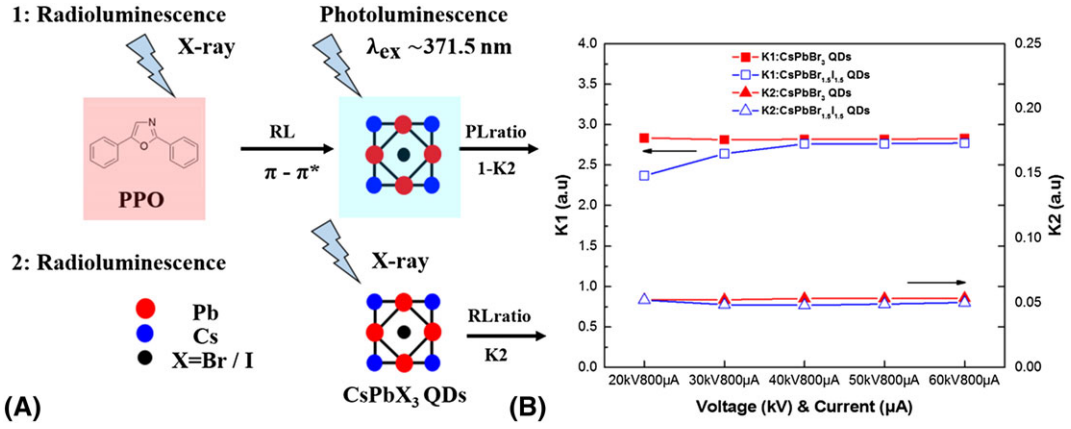

FIGURE 7 A, Schematic of the radioluminescence (RL_{ratio}) and photoluminescence (PL_{ratio}) shares in the quantum dot/2,5-diphenyloxazole (QD/PPO) system. B, K_1 and K_2 in QD/PPO under different X-ray irradiation environments [Colour figure can be viewed at wileyonlinelibrary.com]

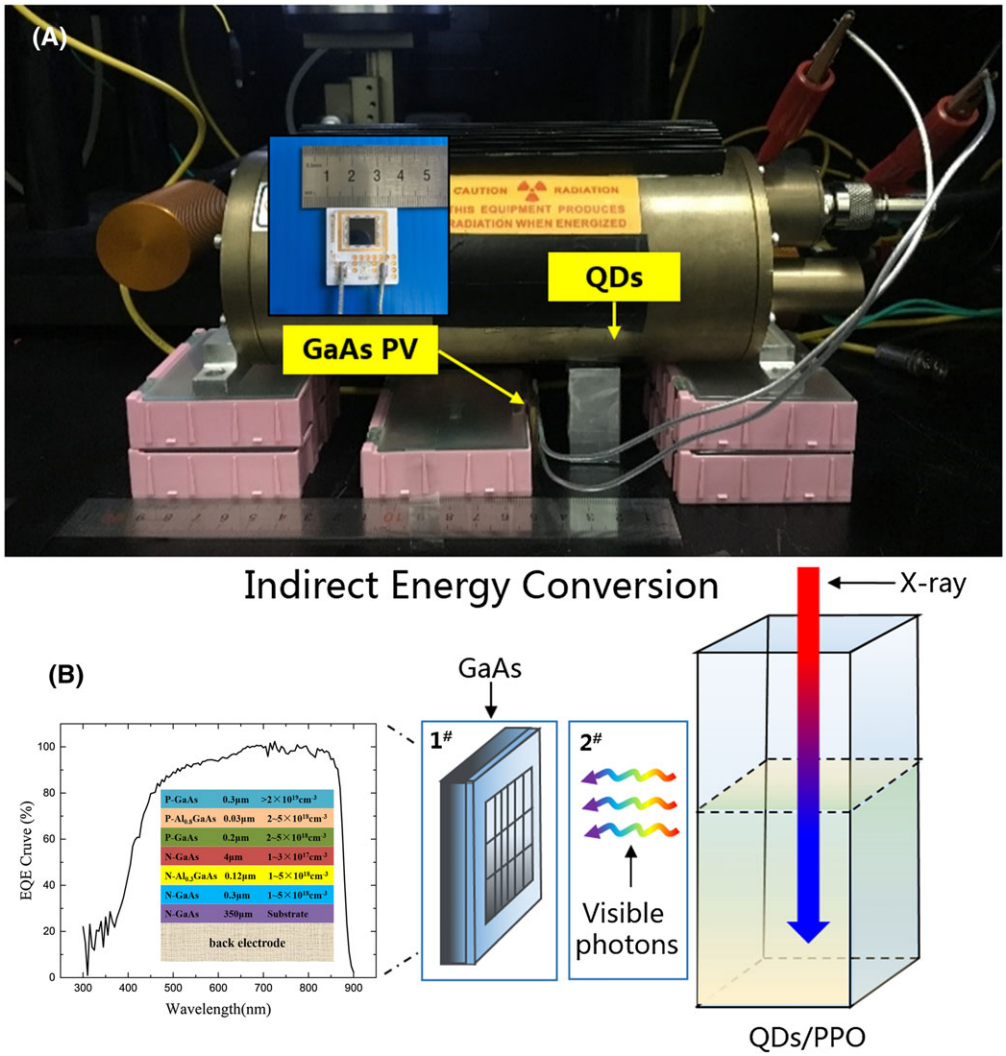

FIGURE 8 A, Physical and B, schematic diagrams of the quantum dot/2,5-diphenyloxazole (QD/PPO) radioluminescent nuclear battery [Colour figure can be viewed at wileyonlinelibrary.com]

experimental method was used to characterize the RL spectra of different fluorescent materials and the normalized RL spectra were obtained. The external quantum efficiency curve of EMCCD was provided by the manufacturer, and the external quantum efficiency curve of GaAs PV was obtained from the test (Figure 12).

The SMFs of the PPO, $CsPbBr_{1.5}I_{1.5}$ QD/PPO, and $CsPbBr_3$ QD/PPO materials were calculated by using the data in Figure 12 and formula 6. The FWHM and peak RL spectra of different fluorescent materials, as well as the SMF for GaAs and EMCCD, are shown in Table 2.

As can be seen from the normalized RL spectra, both types of QDs absorbed all the RL generated by PPO under different X-ray irradiation conditions. The RL emission spectra of QD/PPO systems are determined by the type of QDs. The selection of the 2 QDs ($CsPbBr_{1.5}I_{1.5}$ QDs and $CsPbBr_3$ QDs) RL emission spectra has a more suitable peak position and a narrower FWHM for EMCCD and GaAs PV than before. For EMCCD and GaAs PV, the SMF for QD/PPO systems is nearly twice of that for the PPO system, which are presumed to be the major reason for the substantial gain in optical and electrical properties.

3.6 | Relationship between optical properties and electrical characteristics of radioluminescent nuclear batteries

The relationship between optical performance that refers to EMCCD counts and electrical performance that refers to the maximum output power in QDs/POO and PPO radioluminescent nuclear batteries was established based on the above test results (Figure 13). For radioluminescent nuclear battery, regardless of the type of fluorescent material used, the maximum output power is directly proportional to the fluorescence count.

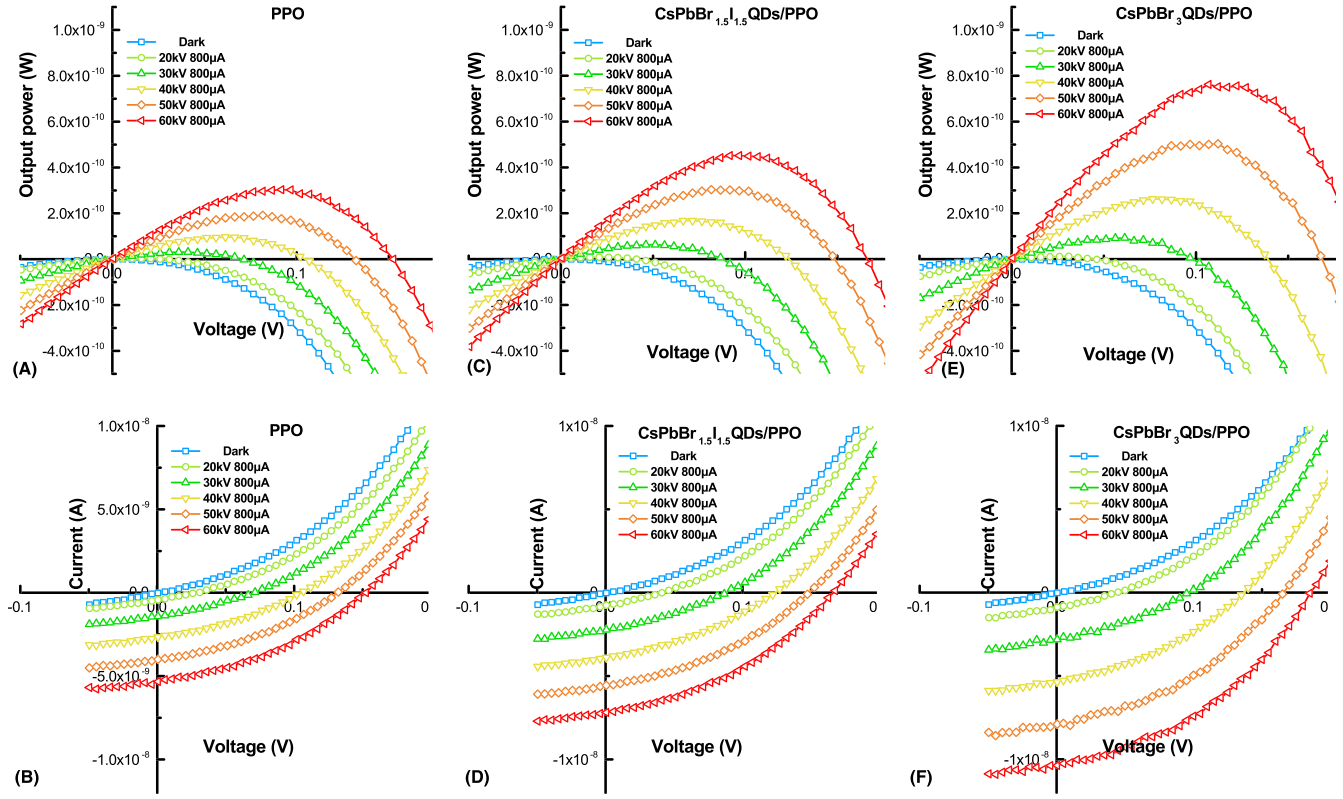

FIGURE 9 *I-V* characteristic curves of the A, 2,5-diphenyloxazole (PPO), C, $CsPbBr_{1.5}I_{1.5}$ quantum dot (QD)/PPO, and E, $CsPbBr_3$ QD/PPO radioluminescent nuclear batteries. *P-V* characteristic curves of the B, PPO, D, $CsPbBr_{1.5}I_{1.5}$ QD/PPO, and F, $CsPbBr_3$ QD/PPO radioluminescent nuclear batteries [Colour figure can be viewed at wileyonlinelibrary.com]

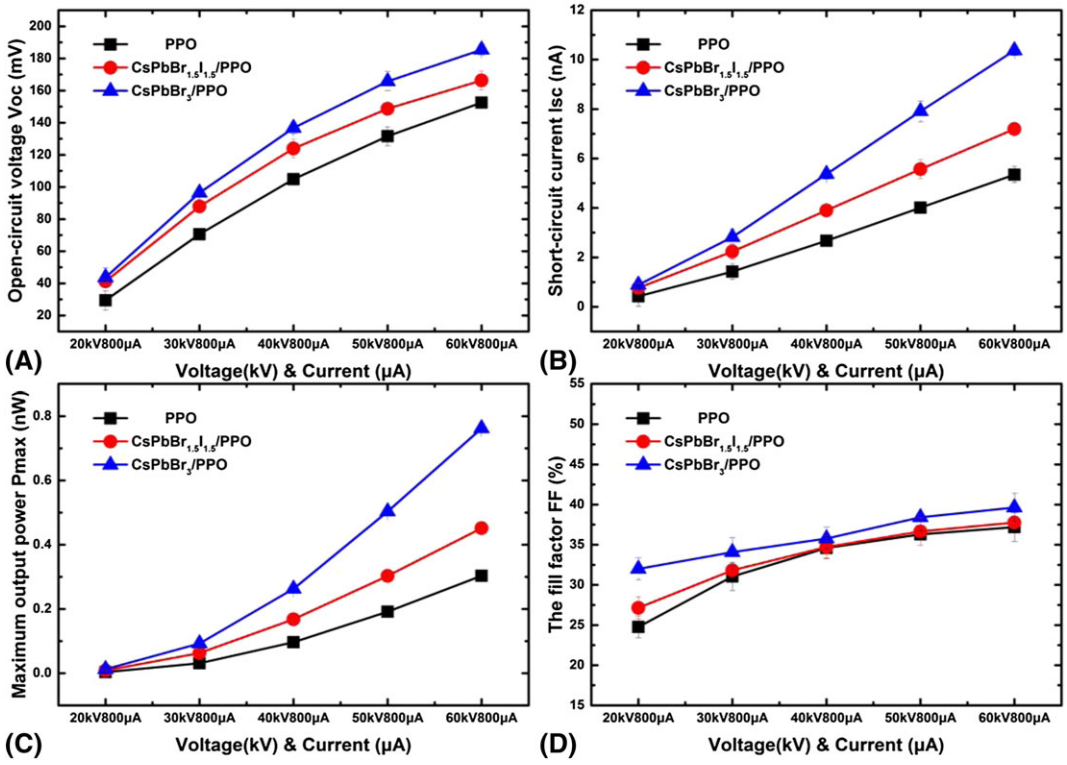

FIGURE 10 A, Short-circuit current (I_{sc}), B, Open-circuit voltage (V_{oc}), C, Maximum output power (P_{max}), and D, fill factor (FF) of the radioluminescent nuclear batteries [Colour figure can be viewed at wileyonlinelibrary.com]

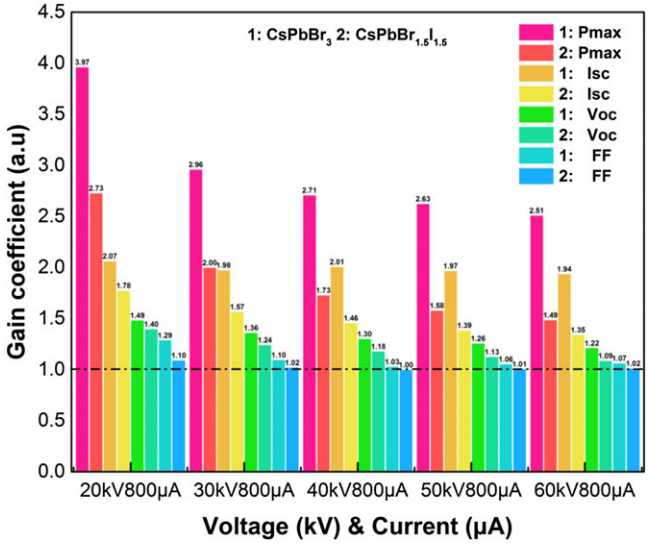

FIGURE 11 Gain coefficients of V_{oc}, I_{sc}, P_{max}, and FF of the quantum dot/2,5-diphenyloxazole radioluminescent nuclear batteries (PPO radioluminescent nuclear battery as a reference) [Colour figure can be viewed at wileyonlinelibrary.com]

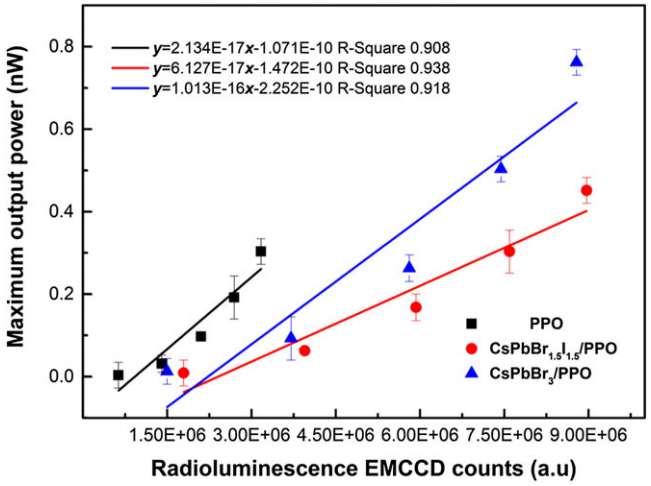

FIGURE 13 Linear relationship between electron-multiplying charge-coupled device (EMCCD) counts and maximum output power of the nuclear radioluminescent battery [Colour figure can be viewed at wileyonlinelibrary.com]

4 | CONCLUSION

$CsPbBr_3$ and $CsPbBr_{1.5}I_{1.5}$ perovskite QDs were synthesized by hot-injection and combined with the PPO as a control. The HRTEM images show that the resulting particle sizes are 7.08 and 8.33 nm. The RL images and the RL spectra of QDs, QD/PPO, and PPO were characterized by using EMCCD, and RL of PPO was completely absorbed by the $CsPbBr_3$ QDs and $CsPbBr_{1.5}I_{1.5}$ QDs. The peak positions of RL spectra changed from 371.5 nm (PPO) to 515.9 nm ($CsPbBr_3$ QD/PPO) and 619.8 nm ($CsPbBr_{1.5}I_{1.5}$ QD/PPO) after spectral regulation. According to EMCCD counts statistics, the QD/PPO system produced 4.79% to 5.35% of RL and nearly 95% of PL.

The fluorescence counts of the RL images in the QD/PPO system are significantly increased. The EMCCD counts in the QD/PPO system increased by ~2.36 to 2.83 times over the POO system. The main reason is that the QD/PPO RL emission peak is in a more sensitive area of the EMCCD external quantum efficiency curve.

The electrical performance of the QD/PPO nuclear radioluminescent battery was significantly improved. The I_{sc} increased by 2.07 to 1.35 times. The V_{oc} increased by 1.49 to 1.09 times. The P_{max} increased by 3.97 to 2.51 times. The FF increased by 1.01 to 1.10 times. The QD/PPO system can improve the RL intensity and regulate the RL spectrum suitable for GaAs external quantum efficiency curve. The SMF of GaAs PV for QD/PPO is approximately 2.24-fold to 2.51-fold compared with PPO.

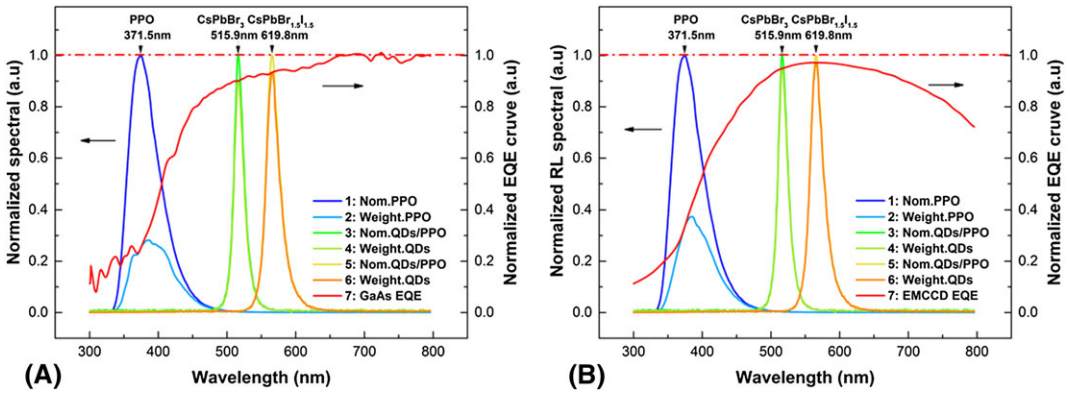

FIGURE 12 A, Normalized radioluminescence spectra of 2,5-diphenyloxazole (PPO), $CsPbBr_{1.5}I_{1.5}$ quantum dot (QD)/PPO, $CsPbBr_3$ QD/PPO, and the external quantum efficiency curve of electron-multiplying charge-coupled device (EMCCD). B, Normalized radioluminescence spectra of PPO, $CsPbBr_{1.5}I_{1.5}$ QD/PPO, $CsPbBr_3$ QD/PPO, and the external quantum efficiency of GaAs [Colour figure can be viewed at wileyonlinelibrary.com]

The selection of QD/PPO as a fluorescent material can significantly improve the overall output performance of the radioluminescent nuclear battery. A linear relationship was found between the optical properties and the electrical properties. The feasibility of using perovskite QDs for the radioluminescent nuclear battery was verified. Perovskite QDs also have excellent application prospects for the (α, β, γ, and X-ray sources) radioluminescent nuclear battery and X-ray imaging technology.

ACKNOWLEDGEMENTS

The authors would like to acknowledge the support of the National Natural Science Foundation of China (grant no. 11505096 and 11675076), the Natural Science Foundation of Jiangsu Province (grant no. BK20150735), the Shanghai Aerospace Science and Technology Innovation Project (grant no. SAST2016112), the Foundation of Graduate Innovation Center in NUAA (grant no. kfjj20170611), and the Priority Academic Programme Development of Jiangsu Higher Education Institutions.

ORCID

Xiaobin Tang http://orcid.org/0000-0003-3308-0468

REFERENCES

1. Saotome Y, Iwazaki H. Superplastic backward microextrusion of microparts for micro-electro-mechanical systems. *J Mater Process Technol*. 2001;119(1-3):307-311.
2. Qiao DY, Chen XJ, Ren Y, Yuan WZ. A micro nuclear battery based on SiC schottky barrier diode. *J Microelectromech Syst*. 2011;20(3):685-690.
3. Siciliani De Cumis M, Farsi A, Marino F, et al. Radiation pressure excitation and cooling of a cryogenic micro-mechanical systems cavity. *J Appl Phys*. 2009;106:1-18.
4. Li H, Liu Y, Hu R, et al. Simulations about self-absorption of tritium in titanium tritide and the energy deposition in a silicon Schottky barrier diode. *Appl Radiat Isot*. 2012;70(11):2559-2563.
5. Landis GA, Bailey SG, Clark EB, Myers MG, Piszczor MF, Murbach MS. Non-solar photovoltaics for small space missions. In 2012 *38th IEEE Photovoltaic Specialists Conference (PVSC)*, pp. 002819–002824, Austin, TX, 2012.
6. Prelas MA, Weaver CL, Watermann ML, Schott RJ, Wisniewski DA. A review of nuclear batteries. *Prog Nucl Energy*. 2014;75:117-148.
7. Prelas M, Boraas M, Aguilar FDLT, Seelig J-D, Tchouaso MT, Wisniewski D. *Nuclear Batteries and Radioisotopes*. Cham, Switzerland: Springer International Publishing; 2016.
8. Sychov M, Kavetsky A, Yakubova G, et al. Alpha indirect conversion radioisotope power source. *Appl Radiat Isot*. 2008;66(2):173-177.
9. Xu ZH, Tang XB, Hong L, Liu YP, Chen D. Structural effects of ZnS:cu phosphor layers on beta radioluminescence nuclear battery. *J Radioanal Nucl Chem*. 2015;303:2313-2320.
10. Kim T, Lee N, Jung HK, Kim JH. Enhancement of energy performance in betavoltaic cells by optimizing self-absorption of beta particles. *Int J Energy Res*. 2016;40(4):522-528.
11. Zhang J, Xuan Y, Yang L. A novel choice for the photovoltaic–thermoelectric hybrid system : the perovskite solar cell. *Int J Energy Res*. 2016;40(10):1400-1409.
12. Wei W, Hu YH. Catalytic role of H_2O in degradation of inorganic–organic perovskite ($CH_3NH_3PbI_3$) in air. *Int J Energy Res*. 2017;41(7):1063-1069.
13. Protesescu L, Yakunin S, Bodnarchuk MI, et al. Nanocrystals of cesium lead halide perovskites ($CsPbX_3$, X = Cl, Br, and I): novel optoelectronic materials showing bright emission with wide color gamut. *Nano Lett*. 2015;15(6):3692-3696.
14. Nikolopoulos D, Valais I, Michail C, et al. Radioluminescence properties of the CdSe/ZnS quantum dot nanocrystals with analysis of long-memory trends. *Radiat Meas*. 2016;92:19-31.
15. Chen W, Liu Y, Yuan Z, et al. X-ray radioluminescence effect of all-inorganic halide perovskite CsPbBr3 quantum dots. *J Radioanal Nucl Chem*. 2017;314(3):2327-2337.
16. Palazon F, Akkerman QA, Prato M, Manna L. X-ray lithography on perovskite nanocrystals films: from patterning with anion-exchange reactions to enhanced stability in air and water. *ACS Nano*. 2016;10(1):1224-1230.
17. Butera S, Lioliou G, Barnett AM. Gallium arsenide ^{55}Fe X-ray-photovoltaic battery. *J Appl Phys*. 2016;119(6):064504.
18. Butera S, Lioliou G, Krysa AB, Barnett AM. Al0.52In0.48P ^{55}Fe x-ray-photovoltaic battery. *J Phys D Appl Phys*. 2016;49(35):355601.
19. Zhang Z-R, Tang X-B, Liu Y-P, et al. GaAs radiovoltaic cell enhanced by Y_2SiO_5 crystal for the development of new gamma microbatteries. *Nucl Instrum Methods Phys Res, Sect B*. 2017;398:35-41.
20. Valais I, Nikolopoulos D, Kalivas N, et al. A systematic study of the performance of the CsI:Tl single-crystal scintillator under X-ray excitation. *Nucl Instrum Methods Phys Res, Sect A*. 2007;571(1-2):343-345.

SUPPORTING INFORMATION

Additional Supporting Information may be found online in the supporting information tab for this article.

How to cite this article: Chen W, Tang X, Liu Y, et al. Novel radioluminescent nuclear battery: Spectral regulation of perovskite quantum dots. *Int J Energy Res*. 2018;42:2507–2517. https://doi.org/10.1002/er.4032